

# Electromagnetic Calorimetry and $e/\gamma$ Performance in CMS

G. Dissertori

on behalf of the CMS ECAL Collaboration

Institute for Particle Physics, ETH Zürich, Switzerland  
e-mail: guenther.dissertori@cern.ch

**Abstract.** The electromagnetic calorimeter of the CMS experiment at LHC will consist of about 76000 Lead Tungstate crystals. Its main purpose is the very precise energy measurement of electrons and photons produced in proton-proton collisions at 14 TeV centre-of-mass energy. A review is given of its main building blocks and its construction status. Then the results of the testbeam campaign in 2002 are discussed. Finally, the overall calibration and reconstruction strategy is outlined.

PACS: CMS ECAL electromagnetic calorimetry crystals

---

## 1 Introduction

Experiments at the Large Hadron Collider (LHC) will study proton-proton collisions at a centre-of-mass energy of 14 TeV, at a maximum design luminosity of  $10^{34} \text{ cm}^{-2} \text{ s}^{-1}$  and a crossing rate of 40 MHz. The main physics goals pursued will be the search for the Higgs boson, which is the missing corner-stone in the Standard Model of particle physics, as well as the search for supersymmetric particles. For a low Higgs mass ( $\lesssim 150 \text{ GeV}/c^2$ ) the golden channel for the Higgs hunt is its decay into two photons, whereas the processes  $H \rightarrow WW$  and  $ZZ$  will be important at higher masses, where the  $W$  and  $Z$  bosons are identified via their leptonic decays. Therefore, it becomes clear that an excellent energy and angular resolution for the detection of electrons and photons is mandatory. In particular, the electromagnetic calorimetry for the future LHC detectors can be benchmarked by considering the Higgs mass resolution  $\sigma_m/m$  in the  $H \rightarrow \gamma\gamma$  channel. The mass resolution is important since at low Higgs masses the detector resolution will completely dominate over the intrinsic Higgs width, and at the same time there will be a very large irreducible QCD background. Since

$$\frac{\sigma_m}{m} = \frac{1}{2} \left[ \frac{\sigma_{E_1}}{E_1} \oplus \frac{\sigma_{E_2}}{E_2} \oplus \frac{\sigma_\theta}{\tan \theta/2} \right], \quad (1)$$

where  $E_{1,2}$  are the energies of the two photons and  $\theta$  their angular separation, it is evident that an excellent reconstruction of the Higgs mass relies both on the energy and angular resolution. A homogeneous crystal calorimeter guarantees a very high energy resolution. In order to take full advantage of its good intrinsic resolution, the magnet coil needed for tracking should not be in front of the

calorimeter, so the calorimeter should be inside the coil. Therefore compactness becomes an issue. Because of the high crossing rate and the high luminosity, leading to about 20 events and approximately 1000 tracks per crossing, further requirements for the calorimeter are a very fast detector response, high granularity and radiation hardness in order to withstand the hazardous environment.

Altogether the above considerations have led the CMS collaboration to opt for a hermetic electromagnetic calorimeter (ECAL) [1] built out of 75848 Lead Tungstate ( $PbWO_4$ ) crystals. These crystals have a short radiation length ( $X_0 = 0.89$  cm) and Molière radius ( $R_M = 2.2$  cm), which allows construction of a compact and highly granular detector. The time constant of the scintillation mechanism (80% of the light emitted within 25 ns) is well adapted to the 25 ns LHC bunch crossing interval, and radiation hardness has been achieved by appropriate doping and growth methods. However, the relatively low light yield necessitates the usage of photo-detectors with intrinsic gain. In addition, the sensitivity of both the crystal and photo-detector response to temperature fluctuations requires a precise control of the temperature stability. These aspects, as well as details of the detector components, will be addressed below.

The energy resolution of a calorimeter is typically parameterized by

$$\frac{\sigma_E}{E} = \frac{a}{\sqrt{E}} \oplus \frac{b}{E} \oplus c, \quad (2)$$

where the CMS target values are 2.7% for the stochastic term  $a$ ,  $b < 200$  MeV for the noise term (for reconstructed energy clusters) and a constant term  $c$  at the 0.5% level. In order to achieve such an excellent resolution, a considerable effort has to go into the careful control of many detector parameters. The stochastic term  $a$  gets contributions from the photostatistics, i.e., the Poissonian statistics of a finite number of photo-electrons collected by the photo-detectors (the effective number of photo-electrons is modified by the excess noise factor  $F$  of the photo-detectors related to the avalanche process), from the fluctuations in the lateral shower containment and the sampling fluctuations of energy deposited among neighbouring crystals. The electronics noise of the readout chain and leakage current in the photo-detectors give the noise term  $b$ . The contributions to the constant term  $c$  are given by the longitudinal shower containment, the non-uniformity in the light production and the precision of the inter-crystal and overall calibration. The latter might be influenced by instabilities and non-uniformities in the detector parameters, such as temperature, or response changes induced by radiation.

In the following, the status of the detector construction is summarized, then the results of the testbeam period in the year 2002 are given, where many of the aforementioned issues related to the detector response and control have been studied. Finally, the basic electron and photon reconstruction issues and the general strategy for the detector calibration are outlined.

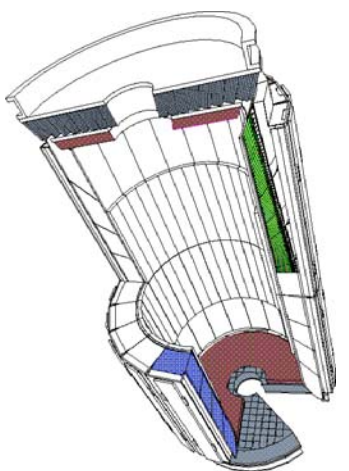


**Fig. 1.** Overall view of ECAL

## 2 Description of the system and construction status

### 2.1 Overall structure

An overall view of the ECAL is given in Fig. 1. It is subdivided in a barrel part (EB) and two endcaps (EE), with in addition a pre-shower detector in front of the latter. The basic goal of the pre-shower is to assist the separation of genuine single and double photon events from  $\pi^0$  decays, by measuring the shower profile between absorber plates with 2mm-pitch silicon strip sensors. A detailed description of the pre-shower detector can be found in Ref. [2].

The barrel electromagnetic calorimeter will have an inner radius of 1.29 m and a granularity  $\Delta\eta \times \Delta\varphi = 0.0175 \times 0.0175$  using 23 cm ( $26 X_0$ ) long crystals with a front face of  $\sim 22 \times 22 \text{ mm}^2$  for a total crystal volume of  $8.14 \text{ m}^3$ . The mechanical design is based on modularity and on the use of high-strength, low-Z materials, where alveolar submodules (Fig. 2(left)) of  $2 \times 5$  fiberglass cells containing individual crystals are the smallest subunits. Such submodules are assembled into modules (Fig. 2(centre)). Super-modules (Fig. 2(right)) consist of four modules held by a U-shaped spine at the outer ECAL radius, and contain about 1700 crystals. The hermeticity has been optimized by tilting the crystal axis by  $3^\circ$  with respect to the direction pointing toward the interaction point. The barrel ECAL covers the pseudo-rapidity region  $|\eta| < 1.48$ .

The ECAL endcaps are built up of identical  $5 \times 5$  crystal "super-crystals", 22 cm long (owing to the presence of the  $3 X_0$  thick pre-shower detector in front) and with  $24.7 \times 24.7 \text{ mm}^2$  front face dimensions. The front face of the calorimeter shall be at a distance of 3170 mm longitudinally from the interaction point along the beam axis. To ensure an hermetic design, the crystals will be oriented toward a point located 1300 mm beyond the interaction point, thus off-pointing to a similar extent as the barrel crystals. An alveolar carbon fiber support structure is foreseen here as well, with the super-modules cantilevered off the front side of "Dee"-shaped, 5 cm thick Aluminum support plates. The EE covers the pseudo-rapidity region  $1.48 < |\eta| < 3.0$ .

The ECAL barrel construction has been split into the mechanical assembly of "bare" super-modules and into the mounting and testing of the cooling and

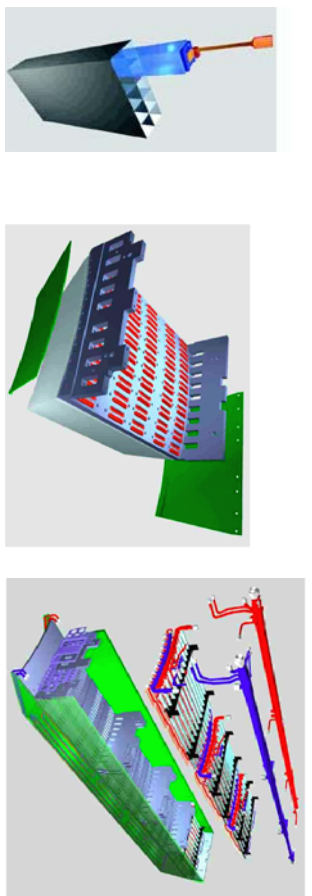


**Fig. 2.** Stages of an ECAL super-module assembly. Left : Alveolar submodule during insertion of the first crystal; Centre : Complete module; Right : Expanded view of a super-module with cooling circuits

readout electronics. In the two Regional Centers, at CERN and in Rome, the module construction is proceeding well, and has achieved the goal of 24 modules ready by the end of 2002. The assembly of bare super-modules has been started, and the completion of 10 such bare super-modules is planned by the end of 2003. By the end of 2004, about 22 super-modules will be completed.

## 2.2 Lead Tungstate crystals

In the production of crystals for the CMS ECAL, the reproducibility of the crystal characteristics is the main goal, with acceptable values in terms of optical parameters as well as resistance to radiation, this last issue being the most critical. The environment for the CMS ECAL is very hostile in this respect, since at the highest luminosity of  $10^{34} \text{ cm}^{-2} \text{ s}^{-1}$  one expects maximum dose rates of around 0.25 Gy/h in the ECAL barrel, values of around 0.30 Gy/h at the barrel-EE interface and 15 Gy/h at  $\eta = 3$ . The hadron flux in the EB calorimeter is expected to reach  $2 \times 10^{13} \text{ n/cm}^2$  for an integrated luminosity of  $5 \times 10^5 \text{ pb}^{-1}$  (equivalent to 10 years of running at LHC). In the EE it will reach  $\sim 10^{15} \text{ h/cm}^2$  with comparable fluxes of charged hadrons and neutrons. However, no damage by neutron irradiation has been seen so far, while crystal transparency is affected by ionizing radiation. It has been shown that the scintillation mechanism is not damaged, nor is the scintillation emission spectrum changed [1]. The small decrease in light output is due to radiation-induced absorption, i.e. to the formation of color centers, which reduce the crystal transparency and which can be due to oxygen vacancies and other imperfections during crystal growth. Because only the transparency is affected, it is possible to monitor the loss in transmission due to irradiation using a light injection system in the calorimeter, and to apply corrections for it.

After completion of the pre-production phase, the crystal production for the ECAL barrel has started at the Bogoroditsk Techno-Chemical Plant (BTCP) in Russia. By now, 16'300 crystals have been received. Some flexibility in the production scenario was anticipated in order to be able to cope with an increased

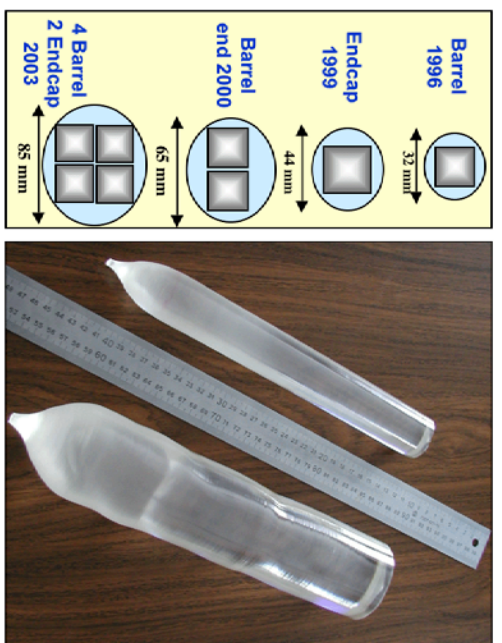


**Fig. 3.** Production of large diameter ingots

demand due to competing markets (ALICE, BTeV, CEBAF and other experiments) and with fluctuations in the production costs. After an initial production step to 65 mm ingots, which allows the cutting of two barrel crystals from one ingot, now all 138 crystal growth furnaces have been upgraded for the production of 85 mm diameter ingots, giving four barrel or two endcap crystals per ingot (c.f. Fig. 3).

Particular attention has been given to the consistency of optical characteristics of crystals obtained with this modified technology with respect to the earlier one. These characteristics will continue to be monitored on all crystals throughout production, along with sample tests for radiation resistance. Preliminary results on the newest production, obtained with a front irradiation at a barrel dose rate of 0.15 Gy/h, yield a damage level always below 5%, which demonstrates that crystals obtained from bigger ingots are also largely tolerant of electromagnetic radiation.

A sample of 100 pre-production EE crystals was delivered by BTCP in the middle of 2001. First, these crystals were characterized in the automated crystal quality control system (ACCOS) at CERN. They are slightly larger in cross-section, shorter, and almost parallelepipedic, compared to the barrel crystals. Ray-tracing studies have predicted that the quasi-absence of tapering should yield EE crystals with a homogeneous light collection efficiency, and thus there is no need for uniformization through depolishing. Because of this, the distribution of light yield is very good, with an average of 10.75 photo-electrons/MeV. However, on the same batch of crystals a distribution of Front-Non-Uniformities (FNUE, for a description it is referred to, e.g., Ref. [4]) in light yield was observed which is shifted with respect to the theoretical expectations and which also shows a secondary bump at high FNUE values. It is assumed that, when crystals will be grown in mass production conditions, the distribution will have

a smaller spread in FNUF values. To verify this, a second batch of 100 crystals was ordered in January 2003, requiring production quality, to check their performance before orders are placed for EE production crystals.

## 2.3 Photo-detectors

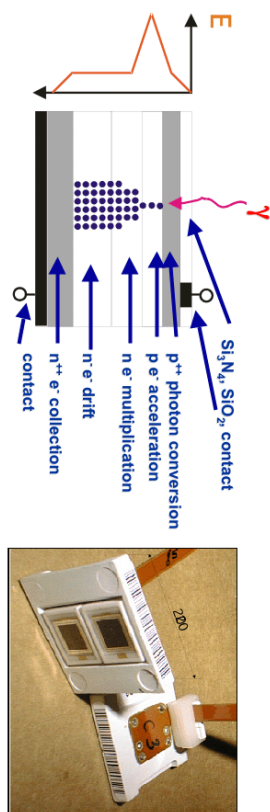


**Fig. 4.** Left : Principle of operation of an APD. Right : Two APDs per capsule

**2.3.1 Avalanche photodiodes (APDs)** As mentioned earlier, because of the relatively low light yield of  $\text{PbWO}_4$ , photo-detectors with intrinsic amplification are needed. In addition, they have to be fast, radiation hard and operate in a strong magnetic field. For the EB these conditions are met by avalanche photodiodes (APDs), an outcome of a 10-year R&D effort between the collaboration and Hamamatsu Photonics. Their principle of operation is shown in Fig. 4 (left).

Two APDs are integrated and connected in parallel within a "capsule" (Fig. 4 (right)), which provides an active area per crystal of  $2 \times 25\text{mm}^2 = 50\text{mm}^2$ . This photo-detection device can have an impact on the energy resolution of the calorimeter through all three terms in the parameterization, eq. (2) : The active area and the quantum efficiency of about 75% contribute to the stochastic term, as well as the excess noise factor ( $F = 2$  at gain  $M = 50$ ), the stability of the operating gain contributes to the constant term via intercalibration effects, and the APD's capacitance and dark current affect the noise term.

Since the capsules, once mounted, will be inaccessible for the whole lifetime of the experiment, very strict Q&A measures are being applied in order to guarantee an APD failure rate below 1/1000. All APDs are subjected to a screening programme which consists in a 500krad pre-irradiation with a  $\text{CO}^{60}$  source and a subsequent annealing and accelerated ageing under bias. Only those devices are retained which fulfil certain pre-defined selection criteria for critical parameters, such as the dark current [5]. A sub-sample is also irradiated with a neutron source.

Once assembled, each capsule is fully characterized [6] w.r.t. its gain, dark current, breakdown voltage, noise and pulse shape; the first three measurements are also repeated after the gluing onto the crystal. More than 50% of the production is already completed by Hamamatsu Photonics.

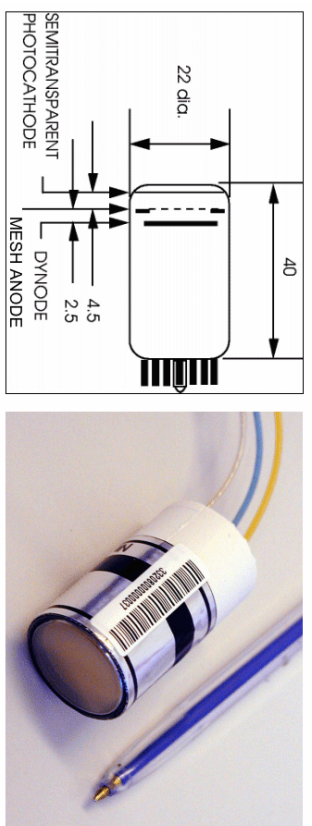


**Fig. 5.** Schematics and view of a VPT

**2.3.2 Vacuum phototriodes (VPTs)** In the ECAL endcaps the radiation levels can be orders of magnitude higher than in the barrel. In particular, the expected neutron flux would be too large for APDs. Therefore the CMS collaboration has chosen to use vacuum phototriodes (VPTs) in the EE. These are single-stage photomultiplier tubes with fine metal grid anodes and UV windows (Fig. 5), giving a quantum efficiency of about 20% at 420nm and an excess noise factor of 3. They have an active area of  $280\text{mm}^2/\text{crystal}$  and provide gains of 8–10. The VPT's response is uniform for the range of angles between their axes and the magnetic field lines.

These devices are produced by the RIE corporation in St. Petersburg, Russia, and by now more than 25% of all VPT's have been delivered. All of them are measured in a magnetic field of  $0 < B < 1.8\text{T}$  and at angular orientations  $-30^\circ < \theta < +30^\circ$ . A sub-sample is also scrutinized at  $B = 4\text{T}$  and  $\theta = 15^\circ$  with an additional faceplate irradiation. So far the measured performance matches the EE design objectives. However, some sorting of VPTs might be needed in order to accommodate an observed spread in anode response.

## 2.4 ECAL readout

The ECAL readout (Fig. 6) has to acquire low-level optical signals with high speed and precision. Digital sums representing the energy deposit in a trigger tower have to be sent to the trigger system every 25 ns. The trigger decision and transmission delays require about 128 bunch crossings, therefore the signal data have to be pipelined during the trigger latency of  $\sim 3\,\mu\text{s}$ .

The high-radiation environment imposes a major design constraint. Each electronics component for the ECAL in the CMS cavern has to withstand levels of radiation ranging from “aerospace” levels of 10 kRad (integrated over the full lifetime) for power supply pass transistors, to up to 1000 times that for detector electronics. At the same time, high-speed (40 MHz) wide dynamic range (30 MeV to 1 TeV) readout requires state-of-the-art design techniques and semiconductor processes. The combination of radiation hardness, high performance and large channel count ( $\sim 75000$ ), thus low unit price, requires the development of full-custom integrated circuits.

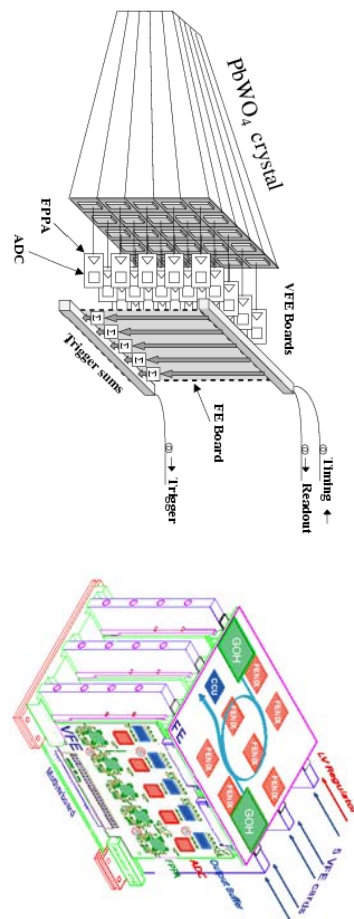


**Fig. 6.** Left : Schematic view of the ECAL readout electronics for  $5 \times 5$  crystals. Right : The arrangement of the front-end electronics into VFE and FE boards.

**2.4.1 Electronics system layout** An ECAL electronics system design review held during the first quarter of 2002 concluded that some of the criteria which were originally driving the system layout are not valid anymore. First, there is now a radiation-hard  $0.25\text{ }\mu\text{m}$  CMOS technology which allows the design and use of ASIC's (Application Specific Integrated Circuit) inside the detector volume at low cost. Second, the cost of optical data link technologies is still very high.

This led to the decision to move the Trigger Primitives Generation (TPG) from the off-detector electronics onto the detector. It implies that the digitized data is read out only upon a Level-1 (L1) trigger accept, which decreases the number of data links and the quantity of off-detector electronics by about a factor of eight as it reduces the overall complexity. The TPG and data storage on the detector will be implemented in a new  $0.25\text{ }\mu\text{m}$  CMOS chip, building on the experience gained in the CMS tracker and pre-shower projects.

This concept is not new and had been considered earlier in the development of the ECAL project but not adopted due to a lack of proven, low cost radiation-hard electronics technology. The functionality of the proposed system is exactly the same as the original system.

The proposed system (barrel and endcaps) will have  $\sim 3000$  data links,  $\sim 6500$  trigger links and  $\sim 3000$  clock and control links, compared to more than  $91000$  links in the original system. In the counting house there will be  $\sim 50$  DCC (Data Concentrator Card) boards,  $\sim 120$  TCC (Trigger Concentrator Card) boards and  $\sim 50$  CCS (Clock and Control System) boards compared to more than  $800$  boards in the original system.

In addition, the revised ECAL system will use the data link technology and the clock and control system developed for the CMS Tracker project. The on-detector electronics will also comprise low voltage regulator (LVR) boards with radiation-hard voltage regulators. This will allow the ECAL project to benefit from the common CMS LV power supply system that transmits power to the detector at 400 V AC, where the conversion to the required low voltages is

performed by radiation and magnetic field tolerant converters. The number of cables required from the control room to the periphery of the detector is thus reduced from  $\sim 1400$  to  $\sim 10$  with a corresponding reduction in cost, installation time and power dissipation. The power dissipated in the detector has been reduced from  $\sim 2.3$  W per crystal to  $\sim 2.0$  W per crystal because, although the voltage regulators add about 35% to the power consumption of the electronics, the number of optical data links has been reduced by a factor of about eight.

**2.4.2 On-detector electronics** The readout electronics on the detector is composed of groups of eight Printed Circuit Boards (PCB) reading  $5 \times 5$  crystals. In the EB this corresponds to a trigger tower and in the EE to a super-crystal. Each group is composed of five Very Front-End electronics (VFE) cards, one Front-End electronics (FE) card, one Low Voltage Regulator (LVR) card and a mother-board.

The signals from the two APD's are pre-amplified and shaped by a transimpedance amplifier with internal shaping, followed by a four-range amplification and logic stage in order to adapt the output to the dynamic range of a 12-bit ADC from Analog Devices, which digitizes the signal every 25 ns. This functionality is integrated into a unique radiation-hard integrated circuit named FPPA (Floating Point Pre-Amplifier). An improved version of the FPPA, called FPPA2001, was received back from fabrication at the end of 2002. Preliminary test results indicate that the main problems of the previous version are solved, which were much too high noise, considerable problems with the pulse shape depending on the input signal size and wrong absolute gain values. They are now corrected. The newly added feature of a variable ADC clock delay is also working correctly and no new problems were discovered. Nevertheless, more detailed tests on a larger sample are ongoing in order to establish the final parameters.

Given the tight timescales, the development of a backup system for the FPPA and ADC had been started, as it was not sure that the FPPA problems could be solved in time. Therefore, two new ASICs have been developed in radiation-hard  $0.25\text{ }\mu\text{m}$  technology. One is a Multi-Gain-Pre-Amplifier (MGPA) which in comparison to the FPPA has no gain switching logic but provides three analogue output signals at three different gains. These three signals are digitized in parallel by a new four-channel, 12-bit 40 MHz ADC with an integrated digital gain switching logic, developed in  $0.25\text{ }\mu\text{m}$  technology. Such a solution would also simplify the low voltage distribution as it requires only two instead of four voltages and it reduces the component cost.

The VFE board has five such readout channels using five FPPA chips and five ADC's (AD9042) or five MGPA and five four-channel ADC's. It feeds the digitized outputs to a FE board (Fig. 6(right)). The FE board contains seven FENIX chips, which provide three functions within a single chip. The data from a row of five crystals is stored until arrival of a L1 accept, the pulse shape data from a row of five crystals are corrected and summed to produce a strip energy. Finally in the case of the EB, the sum of all strip energies is computed to produce the energy deposited in the trigger tower and the fine grain bit as described in the CMS Trigger TDR [3]. In the EE, the five strip sums are transferred to the TCC for summation.

The FENIX chip is developed as an ASIC in  $0.25\mu\text{m}$  technology and has been submitted for fabrication at the beginning of 2003. The TPG algorithms implemented into this chip are those already developed for the off-detector electronics. The trigger data is transmitted to the off-detector electronics through a serial digital data link (five links in the EE) consisting of a GOL (Gigabit Optical Link) serializer chip, a link system based on the CMS tracker link technology, a digital receiver module and a serializer. The link is operated at  $800\text{Mb/s}$ , which is sufficient to complete the transfer of trigger data every 25 ns. On receipt of a L1 accept, the data from the triggered event, that is stored in the memory of the five FENIX chips, is transmitted to the off-detector electronics through a separate serial data link also operated at  $800\text{Mb/s}$ . For every L1 accept, 10 time-slices of data are transmitted off the detector in  $7.5\mu\text{s}$ . The FE electronics will be controlled by the CMS tracker clock and control system. This system uses a  $40\text{MHz}$  digital optical link system, controlled from the off-detector front-end control boards.

**2.4.3 Tests in 2003/2004 and outlook** In 2004 the installation of the readout electronics into the EB super-modules will start and if possible the calibration of at least eight fully equipped super-modules will be performed in the H4 testbeam area. Therefore, the mass production of electronics components has to start in the beginning of 2004. Thus, the year 2003 is the last year to test and validate individual electronics components as well as the system layout. It is planned to have a very extensive test programme throughout 2003. The first super-module (SM0) is being equipped with 100 channels of readout electronics using the FPPA2001 and the AD9042 ADC, including the new cooling system, the mother-boards, LVR boards and FE boards. It will be studied for about six weeks in the H4 testbeam. In addition, 100 channels of readout electronics using the MGPA and the new ADC will be installed into the second super-module (SM1). It will also be tested in the H4 testbeam, in addition to extensive tests with the light monitoring system.

This will allow to compare the performance of the two options in detail and to take a final decision for the system layout during the 3rd quarter of 2003.

## 3 Results from the testbeam in 2002

### 3.1 Setup and goals

In the course of the year 2002 a first prototype of a CMS crystal barrel module was tested in a particle beam. This module, dubbed M0', was the first complete barrel test system, built according to the same construction procedures as the final detector, with all important parameters of each component stored in the construction database.

The M0' module had 100 channels, i.e. 100 crystals disposed in a  $10 \times 10$  matrix, equipped with the prototype FPPAs which were found noisy (c.f. Section 2.4.2). On the other hand, the monitoring laser system and the high-voltage (HV) system were built according to the final specification, whereas the

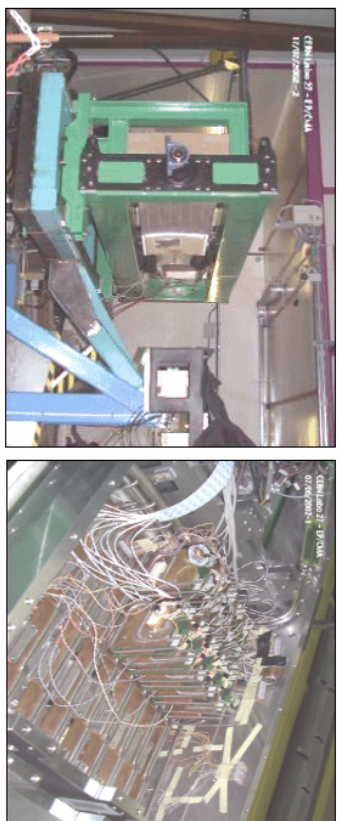


**Fig. 7.** Left : View of the M0' module on the scanning table. Right : VFE cards for 100 channels

LV system, the cooling system, and the detector control system (DCS) were development prototypes.

The module was installed on a remotely controlled calibration table which allowed to center each crystal in turn in the beam. An automatic scanning procedure was also tested which should ultimately fully automatize the calibration of the completed super-modules. Auxiliary equipment such as hodoscopes and multi-wire proportional chambers were installed as well. The installation was completed in time for the first beam on July 29th. A long test period of some 40 days of beam followed in the months of August and September, during which over 10'000 runs were taken, totalling about 500 Gbytes of data recorded on disk. To allow for an extended study of the stability of the whole system (voltage, temperature, dark current, laser monitoring) the data taking was pursued for several weeks after the beam was turned off.

Most of the time the crystals were tested with electrons. An energy scan was done with 20, 30, 50, 80, 120, 150, 180, 200, 250, and 280 GeV electrons, with the beam centered on each crystal. Calibrations were done at 50 GeV, at 80 GeV, at 120 GeV (repeated 12 times for a check of the stability), at 200 GeV (for two crystals), and finally at 250 GeV for 30 crystals. The influence of the beam position was studied by moving the beam in 1 mm steps across six crystals.

Since the crystals were equipped with a noisy and not final version of the readout electronics, the major focus has rather been on system tests than on physics and calibration studies. The objectives were thus

- first test of a large scale system, in particular regarding the VFE, HV, LV, DAQ, DCS and the cooling of a large number of channels;
- test of the system readiness for the testbeam in 2003 and the calibration runs in 2004, with emphasis on the DAQ and online software, the moving table, the understanding of the laser monitoring system, stability checks of the laser and the cooling systems and the preparation for offline analysis;
- measurements of the crystal behaviour under irradiation, and comparison

of the crystal response to laser light and beam particles for a large number of crystals;

- comparison of the crystal light yield as obtained from the laboratory measurements and from the beam data.

In the following a few of these items are described in more detail.

### 3.2 Stability checks

An excellent temperature stability of the calorimeter system is mandatory for the following reasons : the light yield of  $PbWO_4$  crystals shows a strong temperature dependence, with a temperature coefficient of  $-2\%/\text{ }^{\circ}\text{C}$  at  $18\text{ }^{\circ}\text{C}$ . Since the light yield will not be monitored directly, it has to be ensured that the temperature of the crystal volume is kept constant in order to minimize the impact on the intercalibration precision and thus on the resolution. Furthermore, the gain of the APDs is also very sensitive to temperature fluctuations, with a temperature coefficient of  $dM/dT = -2.4\%/\text{ }^{\circ}\text{C}$ . These arguments result in the requirement for the water cooling system to guarantee a long term temperature stability of the crystal volume and the APDs below the  $0.1\text{ }^{\circ}\text{C}$  level, in order to be able to meet the target values for the energy resolution. Here "long term" can be understood to correspond to at least a period between two in-situ calibrations.

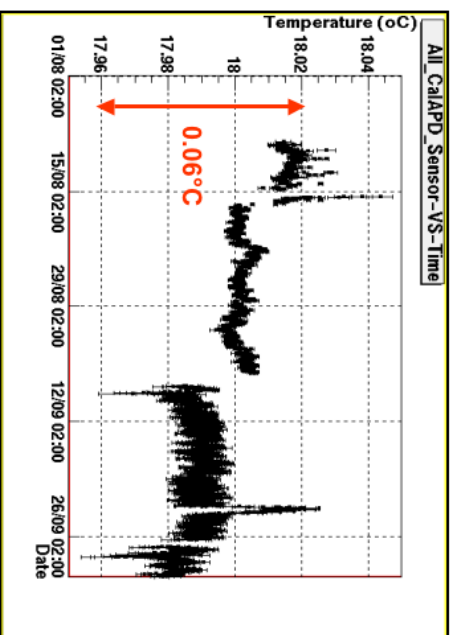


**Fig. 8.** Temperature measured on APDs over a period of two months

The temperature stability of the M0' module has been extensively monitored with a considerable number of temperature sensors installed on the front thermal screen below the crystals (far side w.r.t. the electronics), on the grid which separates the crystals and the electronics and in the capsules close to the APDs. Figure 8 illustrates the temperature measured on the APDs for a period of two months, showing a stability well below the  $0.1\text{ }^{\circ}\text{C}$  limit. The small steps that can be seen in the figure are due to known changes of the system or due to a power

cut. Similar encouraging results have been obtained for all monitored regions of the module. In particular, it has been shown that the large temperature steps in the electronics components induced by powering on or off are not transmitted to the APDs and the crystals. These results have given confidence that the planned cooling system will meet the requirements.

### 3.3 Irradiation studies

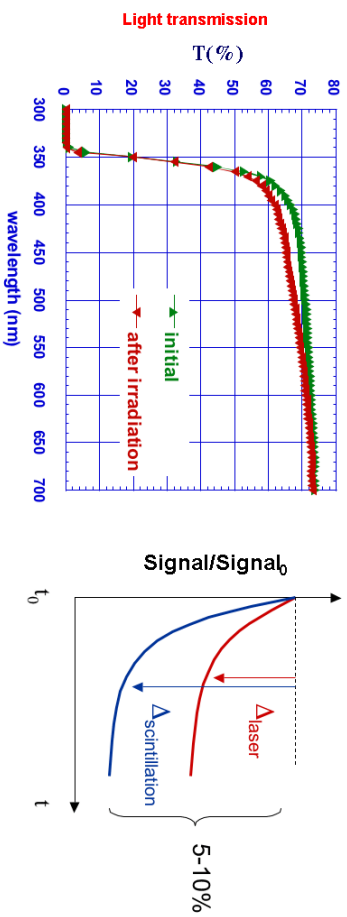


**Fig. 9.** Left : Loss in scintillation light transmission by irradiation as a function of wavelength. Right : Expected behaviour of the crystal response to laser light and to particles under irradiation.

As mentioned in Section 2.2 and illustrated in Fig. 9 (left), irradiation of the crystals results in a reduction of scintillation light transmission. In order to correct dynamically (between calibrations with physics events) the calibration constant of each crystal for this effect, a laser monitoring system will be installed [7]. It distributes laser light of three frequencies through a two-level fanout system with cross-verification by precision radiation-hard PN diodes at each level, and eventually to each crystal via a radiation-hard optical fiber. The basic idea is that the loss of the signal from the laser light follows that from particles according to a ratio  $R = \Delta_{\text{scintillation}}/\Delta_{\text{laser}}$  (c.f. Fig. 9 (right)) which is sufficiently linear and uniform between crystals.

With the Mo<sup>9</sup> module it has been possible to measure  $R$  on a sample of 19 production crystals. The response of the crystals to high dose rates was investigated in depth by irradiating them with an intense beam of 120 GeV electrons over periods of several hours, the cumulated dose reaching between 2 and 8 Gy. The irradiation and subsequent recovery were monitored by means of a blue light laser, corrected to take into account variations of light yield as measured by the reference PN diode. As the laser monitoring runs are taken between the particle runs, an interpolation was done taking the dose into account. The result is shown as a fit to the ratio  $S/S_0$  vs.  $R/R_0$ , where  $S$  is the signal obtained with electrons and  $R$  the signal obtained with the laser,  $S_0$  and  $R_0$  being the signals before irradiation. The relationship  $S/S_0 = (R/R_0)^\alpha$  is fitted to the data with

$\alpha$  as free parameter. As an example the results obtained for one of the crystals are shown in Fig. 10 (left). The fitted parameter  $\alpha = 1.55$  is measured with a precision of 3%. The drop in electron signal is about 5% for a cumulated dose of 2.8 Gy, the corresponding drop for the laser signal is about 3%.

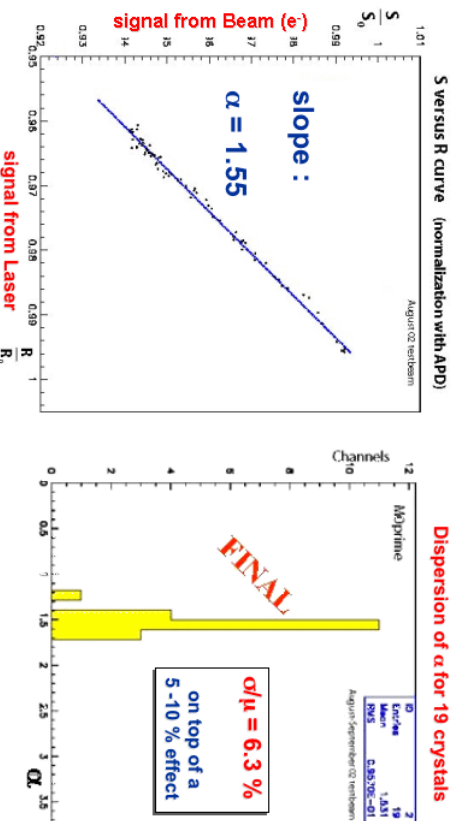


**Fig. 10.** Left : Correlation between the signal from 120 GeV electrons in one crystal and the signal from laser light injection. Right : Dispersion of the parameter  $\alpha$  for 19 crystals.

Figure 10 (right) shows the dispersion of the exponent  $\alpha$  measured for all 19 crystals. Very good uniformity is found with a spread of  $\sigma/\mu = 6.3\%$ .

Two crystals were submitted to repeated irradiations interspersed with periods of recovery, simulating the conditions they will meet in CMS during LHC beam periods and alternated refills. The results were analysed for one crystal only, as the drop in signal response was too small for the second one. For the analysed crystal the ratio  $S/S_0$  was also plotted as a function of the ratio  $R/R_0$ , and a fit to the data points gave the same value for the parameter  $\alpha = 1.6$ , both for the two irradiations and for the recovery.

Clearly these results need to be further substantiated, the statistics must be increased significantly, and the already good stability of the monitoring has to be improved. This will be one of the goals to be reached in 2003.

### 3.4 Crystal intercalibration

As described in more detail in Section 4.2, several steps will be undertaken in order to improve the precision of the crystal intercalibration from an original 5 – 6% to the final goal of 0.5%. This initial value of 5 – 6% was estimated [8] to be obtained from systematic light yield (LY) measurements in the laboratory and the comparison to a reference crystal. The testbeam in 2002 allowed to verify this further by comparing the LY measurements from the lab with those

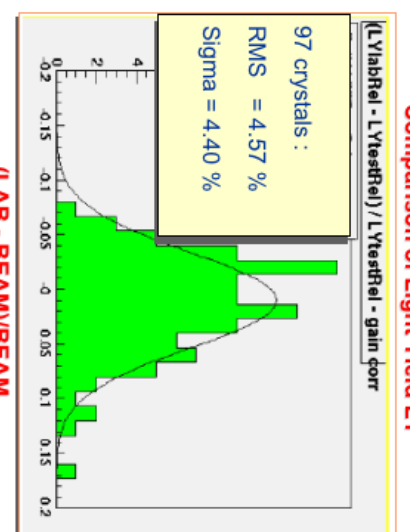


**Fig. 11.** Comparison of crystal light yield as obtained from laboratory measurements and from electron beam data.

obtained with the electron beam. In order to obtain the LY from the beam data, also the APD and pre-amplifier gain values have to be known precisely. Figure 11 shows the relative difference between the values obtained for 97 crystals from the beam and lab measurements. It turns out that the achievable intercalibration precision is even better than the anticipated 5–6%, namely around 4.5%, which constitutes an important basis for the further calibration improvements by *in situ* methods, in particular in view of the fact that not all 36 super-modules will be calibrated in a testbeam, due to the accelerator schedule at CERN which foresees no beams for the whole of 2005.

## 4 Performance of $e/\gamma$ reconstruction and calibration

### 4.1 Reconstruction issues

After a L1 electron trigger [3] decision the background is dominated by jets where a single  $\pi^0$  takes a large fraction of the jet transverse energy. In order to reduce this background an online reconstruction and selection of physics objects will be performed using the CMS High Level Trigger (HLT), described in detail in [9]. This can be achieved with great flexibility using a single online CPU farm of approximately 2000 processors and running the same object-oriented environment and code as the offline software.

Here we concentrate on electron reconstruction because the target transverse momentum cuts and thresholds for triggering on electrons are much lower than those for photons. Photons, at significantly higher transverse momenta, are adequately reconstructed with the electron algorithms. The electron/photon HLT selection consists of three stages :

**4.1.1 Level-2** The first step is to perform a clustering of the energy deposits in a region specified by the L1 trigger and the estimation of the electron's energy and position from this information. In the barrel section this involves the energy deposited in the crystals alone, in the endcap energy is also deposited in the pre-shower detector.

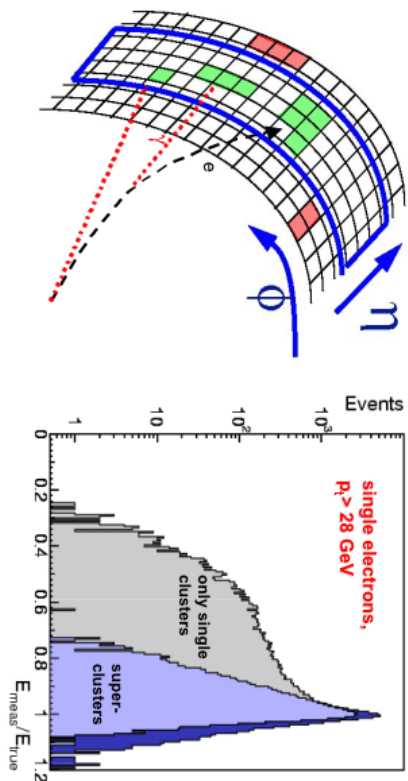


**Fig. 12.** Left : Illustration of Bremsstrahlung recovery in a  $\phi$  road. Right : Recovery of electron energy by reconstructing clusters of clusters (super-clusters)

Because of the tracker material between the interaction point and the ECAL the bending of the electron in the 4T magnetic field results in a spray of energy reaching the ECAL (Fig. 12 (left)). The recovery of this energy loss due to Bremsstrahlung is extremely important, since for an electron with  $p_T = 35$   $\text{GeV}/c$  at  $\eta < 1.5$  it amounts to 43.6% of its energy, on average. Fortunately, the spreading of this spray is, to a good approximation, only in the  $\phi$ -direction. Therefore the electron energy can be collected by making a cluster of clusters (super-cluster) along a  $\phi$  road. In the EB a Hybrid algorithm [10] attempts to use the  $\eta - \phi$  geometry of the crystals to exploit the knowledge of the lateral shower shape in the  $\eta$  direction, while searching dynamically for separated energy in the  $\phi$  direction. In the EE the energy deposited in the pre-shower detector needs to be added to the crystal clusters. Figure 12 (right) illustrates the effect on the energy resolution due to this Bremsstrahlung recovery. The achieved energy resolution for electrons with  $p_T = 35$   $\text{GeV}/c$  amounts to  $\sigma_{\text{Gauss}}/\mu = 1.06\%$  and  $\sigma_{\text{eff}}/\mu = 2.24\%$ , where  $\mu$  indicates the mean value of the  $E_{\text{meas}}/E_{\text{true}}$  distribution,  $\sigma_{\text{Gauss}}$  stands for the central gaussian width and  $\sigma_{\text{eff}}$  for the half width containing 68.3% of the distribution. The corresponding numbers for the endcaps are  $\sigma_{\text{Gauss}}/\mu = 1.23\%$  and  $\sigma_{\text{eff}}/\mu = 2.11\%$ .

**4.1.2 Level-2.5** The energy-weighted average impact point of the supercluster is propagated back to the nominal vertex point and associated hits are

looked for in the pixel detector. If at least two pixel hits are found, the candidate is classified as an electron, otherwise it is classified as a photon.

This matching of super-clusters to hits in the pixel detector is a very powerful tool to reject jet background to electrons. It relies on the following principle. The energy weighted average impact point of an electron and the bremsstrahlung photons it has radiated, is precisely where a non-radiated electron would have impacted. This point can be propagated back through the magnetic field in order to obtain an estimate of the direction of the electron/positron at the vertex, and the hit positions expected in the pixel detector. Since most of the tracker material lies after the pixel detector, most electrons do not radiate significantly before it, and most photons conversions take place after it.

**4.1.3 Level-3** For electrons, tracks are reconstructed and cuts are applied on the ratio of the super-cluster energy to the track momentum and on the difference in pseudo-rapidity,  $\eta$ , between the extrapolated track and the super-cluster position. Isolation requirements are made for both electrons and photons.

**4.1.4 Performance** Detailed performance numbers of this online reconstruction and selection in terms of the electron and photon rates output by the HLT at both low and high luminosity can be found in Refs. [9] and [11]. For example, at low luminosity ( $2 \times 10^{33} \text{ cm}^{-2}\text{s}^{-1}$ ) a total rate of 33 Hz for single electrons is expected, with 10 Hz coming from  $W \rightarrow e\nu$  and the remainder from background. The single and double photon rates are 4 and 5 Hz, respectively. The efficiency for  $H \rightarrow \gamma\gamma$  for  $m_H = 115 \text{ GeV}/c^2$  at low luminosity after the complete selection chain is 77% for events with both photons in the fiducial region, and 84% for events for which the photons also pass the offline  $p_T$  cuts to be used for Higgs searches.

## 4.2 General calibration strategy

In order to achieve the goal of a 0.5% constant term in the energy resolution a major effort has to go into the best possible intercalibration of the crystals. The intercalibration uncertainty enters directly into this constant term with very little scaling, because most of the energy goes into a single crystal.

The calibration procedure will rely on several steps, namely a pre-calibration using laboratory measurements of the crystal light yield, giving already a precision of 4.5% as shown in Section 3.4. Then a sub-set of all super-modules will be calibrated using the H4 testbeam area at CERN, and it is expected that the precision with which the intercalibration constants obtained in the testbeam can be transported to the final CMS detector will be better than 2%. The final precision of 0.5% will be reached by in-situ calibration with physics events as described below, together with the continuous monitoring of the variations in crystal transparency due to irradiation using a laser system. The latter has been described in Section 3.3. More detailed descriptions of the envisaged calibration procedures can be found in Refs. [12] and [13].

**4.2.1 In-situ calibration** A first fast intercalibration will be performed exploiting the  $\phi$ -symmetry of the energy deposition in minimum-bias events [14]. The basic idea is that the total transverse energy deposited from a large number of events is the same for all crystals at a fixed pseudo-rapidity  $\eta$ . This allows the correction of the transverse energy sum (over many events) in a single crystal to the average of this sum over all crystals in a  $\phi$  ring with the same  $\eta$ , and thus to reduce the number of calibration constants from about 60'000 in the barrel to 170, corresponding to the number of rings. With a simulation of 18 million minimum-bias events it has been shown that an intercalibration precision of about 2% can be achieved, and that the method can also be applied to the endcaps (Fig. 13 (left)).

The basic limitation of this method is the non-homogeneity of the tracker material, which leads to asymmetry in  $\phi$ . With an increased knowledge of the tracker material distribution the precision might be improved to about 1% over the whole barrel region, but there remain drawbacks due to non-Gaussian noise (spikes) and to the large lever arm of the extrapolation to high energies. Nevertheless, with a L1 bandwidth of 1kHz assigned to minimum-bias events, handled by the HLT farm, the above mentioned precision could be reached within a few hours only. The method will be studied further by investigating its application to jet triggers. The final in-situ intercalibration will be performed with  $Z \rightarrow e^+e^-$  decays in order to obtain the intercalibration in  $\eta$  and the absolute energy scale. With the expected trigger rates a few days of data taking should suffice to accumulate the necessary statistics.

Once the tracker is fully operational, a calibration can be performed using the measurement of energy and momentum ( $E/p$ ) in semileptonic  $W$  decays,  $W \rightarrow e\nu$ , based on the data accumulated over roughly a period of several weeks to a few months (in order to have sufficient statistics in every crystal, c.f. Fig. 13 (right)). One of the issues is the deconvolution of the calibration constants from the cluster of energy deposits and the constraint from the momentum measured in the tracker. However, efficient algorithms have been developed and also used in the past, as discussed in Ref. [12].

## 5 Summary and conclusions

The construction of the CMS ECAL is progressing well, with important technological improvements regarding the production of larger ingots in order to enhance the crystal yield, and with more than 50% of the APDs and more than 25% of the VPTs already delivered.

The electronics readout scheme has undergone a major redesign, by moving the components for the trigger primitive generation from the counting house onto the detector, thus reducing considerably the number of optical data links, by keeping the same functionality. The project has been characterized by remarkable progress in view of the pressure due to high risk and short time scales. In addition, a new version of the FPPA chip has been delivered, and an alternative chip set w.r.t. the FPPA and the ADC from Analog Devices has been developed in  $0.25\mu m$  technology. A decision on the final solution is expected for the 3rd quarter of 2003.

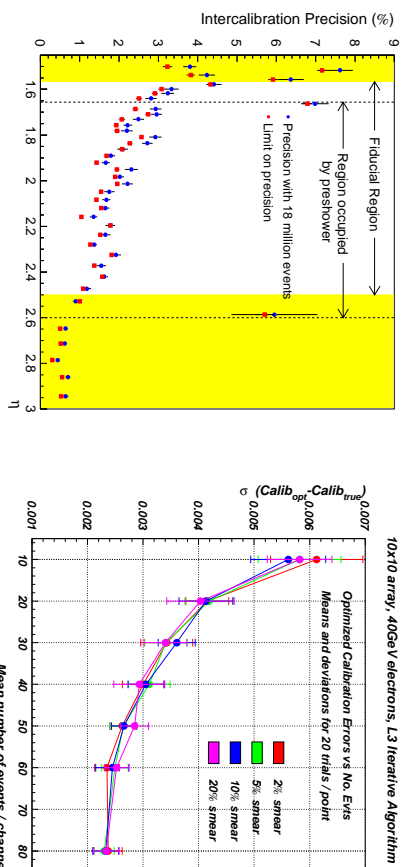


**Fig. 13.** Left : Intercalibration precision at large  $\eta$  which can be obtained with 18 million minimum-bias events and the limit on the intercalibration precision; Right : Calibration precision using  $W \rightarrow e\nu$  decays as a function of the number of events per crystal.

The testbeam campaign in 2002 has given important insights into the system properties of a module with 100 channels equipped with readout electronics. Very encouraging results have been obtained regarding the temperature stability, the laser monitoring and the corresponding follow-up of the variations in light yield due to irradiation, as well as the crystal intercalibration obtained from light yield measurements in the laboratory and confirmed with the testbeam data.

Finally, the relevant issues for the electron and photon reconstruction have been outlined, with the recovery of the energy loss due to bremsstrahlung in the tracker material being of major importance. The best possible intercalibration between crystals will be obtained in several steps, from the intercalibration with laboratory and testbeam measurements to the in-situ calibrations using minimum-bias events and semileptonic  $Z$  and  $W$  decays.

The status of the pre-shower detector has not been described in detail in this report. Nevertheless, excellent progress has been achieved. The active part of the detector consists in 4300 micromodules, based on  $6.3 \times 6.3 \text{ cm}^2$  silicon sensors with 32 strips. Already 25% of these silicon sensors have been produced. The PACE3 and K-chips for the front-end electronics have been redesigned in  $0.25\mu\text{m}$  technology and submitted in March 2003. They will be tested in summer 2003. During this year large mechanical pieces will also be fabricated, and the full-scale production of micromodules is scheduled to start in mid-2004.

## Acknowledgements

I am grateful to all my colleagues from the CMS ECAL collaboration who helped me in the preparation of this presentation. Furthermore I would like to thank the organizers of the symposium.

## References

1. The CMS Collaboration, *CMS Electromagnetic Calorimeter Project - Technical Design Report*, CERN/LHCC 97-33 (1997), CERN, Geneva, Switzerland, 1997.
2. E. Tounnefer, *The Preshower Detector of CMS at LHC*, presentation at the 8th Pisa meeting on advanced detectors, Elba, Italy, May 21-27, 2000; CMS CR-2000/010.
3. The CMS Collaboration, *CMS The TriDAS Project - Technical Design Report*, CERN/LHCC 2000-38 (2000), CERN, Geneva, Switzerland, 2000.
4. M. Diemoz, *The Electromagnetic Calorimeter of the CMS Experiment*, presentation at the 8th Topical Seminar on Innovative Particle and Radiation Detectors Siena, Italy, 21-24 October 2002, CMS CR-2003/003.
5. R. Rusack, *Avalanche Photodiodes for the CMS Lead tungstate Calorimeter*, presentation at CALOR2002, Caltech, 25-30 May 2002.
6. P. Depasse et al., *A Validation Program for the CMS ECAL Photodetection Capabilities*, CMS Internal Note, CMS IN-2000/013.
7. CMS-Saclay group, M. Déardin et al., *The CMS-ECAL Monitoring System : Data Generation, Acquisition and Processing at LHC*, CMS Internal Note, CMS IN-2002/012.
8. F. Cavallari et al., *Test-beam Results on the Performance of Two Matrices of PbWO<sub>4</sub> Crystals for the CMS ECAL and Comparison with Laboratory Measurements*, CMS Internal Note, CMS IN-2001/033.
9. The CMS Collaboration, *CMS The TriDAS Project - Data Acquisition and High Level Trigger*, CERN/LHCC 2002-26, CMS TDR 6.2, Geneva, Switzerland, 2002.
10. E. Meschi et al., *Electron Reconstruction in the CMS Electromagnetic Calorimeter*, CMS Note 2001/034.
11. C. Seez, *The CMS Trigger System*, proceedings of the LHC symposium, Fermilab, May 2003; CMS CR-2003/008.
12. R. Paramatti, *Calibration of the CMS Electromagnetic Calorimeter*, presentation at the 8th Topical Seminar on Innovative Particle and Radiation Detectors Siena, Italy, 21-24 October 2002; CMS CR-2003/002.
13. D. Futyan, *In-Situ Calibration of the CMS Electromagnetic Calorimeter*, presentation at the Lake Louise Winter Institute, Lake Louise, Canada, 16-22 February, 2003; CMS CR-2003/005.
14. D. Futyan and C. Seez, *Intercalibration of ECAL Crystals in Phi Using Symmetry of Energy Deposition*, J. Phys. **G29** (2003) 1299; CMS Note 2002/031.

<http://link.springer.de/link/service/journals/10105/index.html>